Supporting Information

Hybrid Device Architecture using Plasmonic Nanoparticles, Graphene Quantum Dots and Titanium Dioxide for UV Photodetectors

Sundar Kunwar[1], *Sanchaya Pandit*[1], *Rakesh Kulkarni*[1], *Rutuja Mandavkar*[1], *Shusen Lin*[1], *Ming-Yu Li*[2] *and Jihoon Lee*[1]*

[1]Department of Electronic Engineering, College of Electronics and Information, Kwangwoon University, Nowon-gu Seoul 01897, South Korea

[2]School of Science, Wuhan University of Technology, Wuhan, Hubei 430070, China

E-mail: jihoonlee@kw.ac.kr

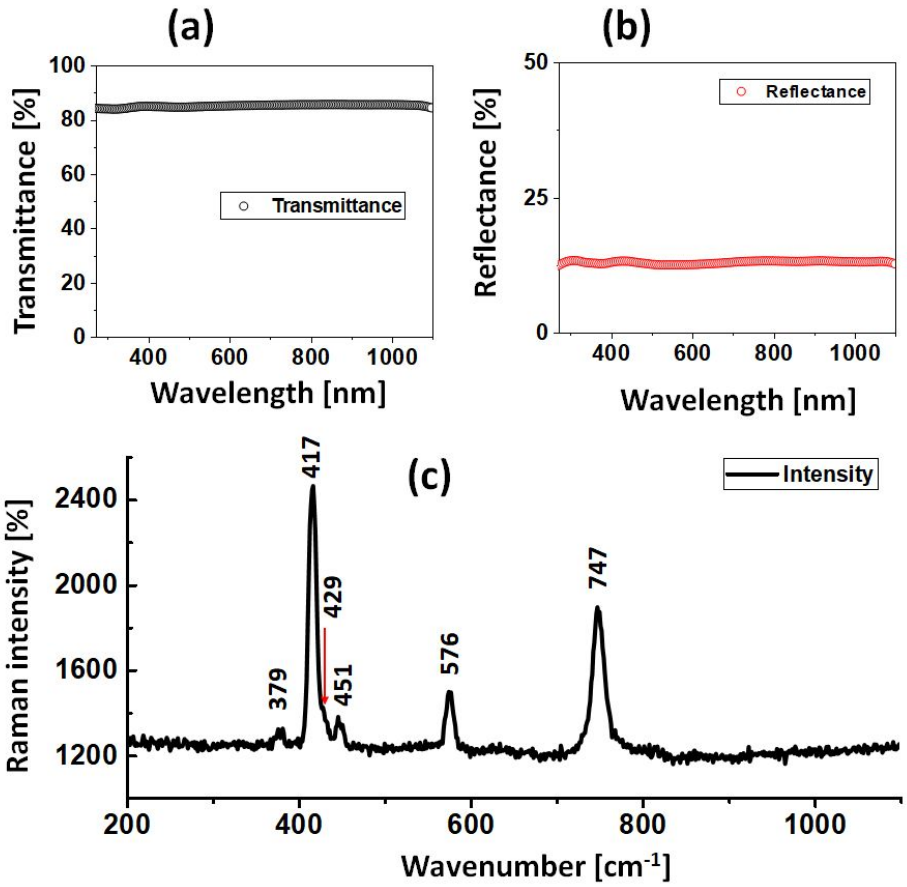

Figure S1. (a) – (b) Transmittance and reflectance spectra of bare sapphire (0001) in the UV-VIS-NIR regions. The transmittance and reflectance spectra were measured in the normal incidence. The bare sapphire exhibited a broadband transmittance and reflectance of ~ 86 and 14 % respectively in between 250 - 1100 nm. The sapphire substrate was chosen for the growth of plasmonic NPs because of their high thermal conductivity and high stability. Furthermore, due to the high optical transparency and low loss in the broad electromagnetic spectrum range, the optical properties of the NPs can be easily extracted. (c) Raman spectra of bare sapphire (0001) by the excitation of 532 nm laser. The active Raman modes of bare sapphire (0001) were at 379 (E_g), 417 (A_{1g}), 429 (E_g), 451 (E_g), 576 (E_g) and 747 (E_g) cm^{-1} [1]. The Raman analysis of hexagonal-rhombohedral c-plane sapphire (0001) showed only sapphire peaks, indicating no contamination or impurity on the substrate.

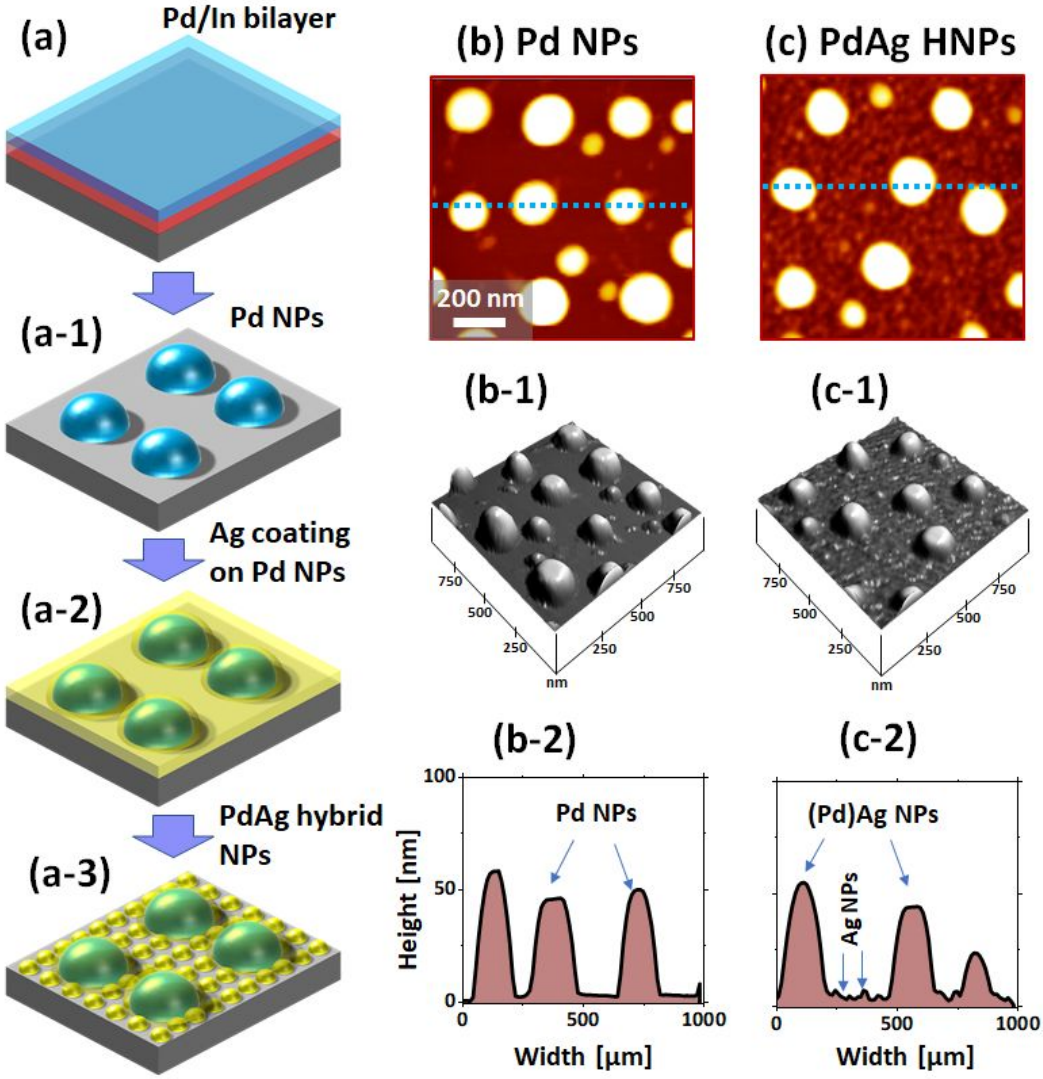

Figure S2. (a) Schematic illustration of the fabrication of PdAg hybrid nanoparticles (HNPs) on sapphire (0001). (a-1) Formation of pure Pd NPs by the dewetting of Pd_{5nm}/In_{5nm} bilayer along with the sublimation of In atoms. Here, the In layer was introduced for the enhancement of Pd atoms diffusion such that well isolated and regular shape of Pd NPs can be obtained after dewetting and sublimation of In at high temperature. (a-2) Deposition of 5 nm thick Ag overlayer on the Pd NP template. (a-3) Evolution of PdAg HNPs surrounded by the tiny Ag NPs. (b) AFM top-view of monometallic Pd NPs fabricated from Pd_{5nm}/In_{5nm} bilayer at 800 °C. (c) AFM top-view of PdAg HNPs fabricated at 600 °C by the deposition of 5 nm thick Ag layer on the Pd NPs template. (b-1) - (b-2) & (c-1) - (c-2) Corresponding AFM side-views and line-profiles.

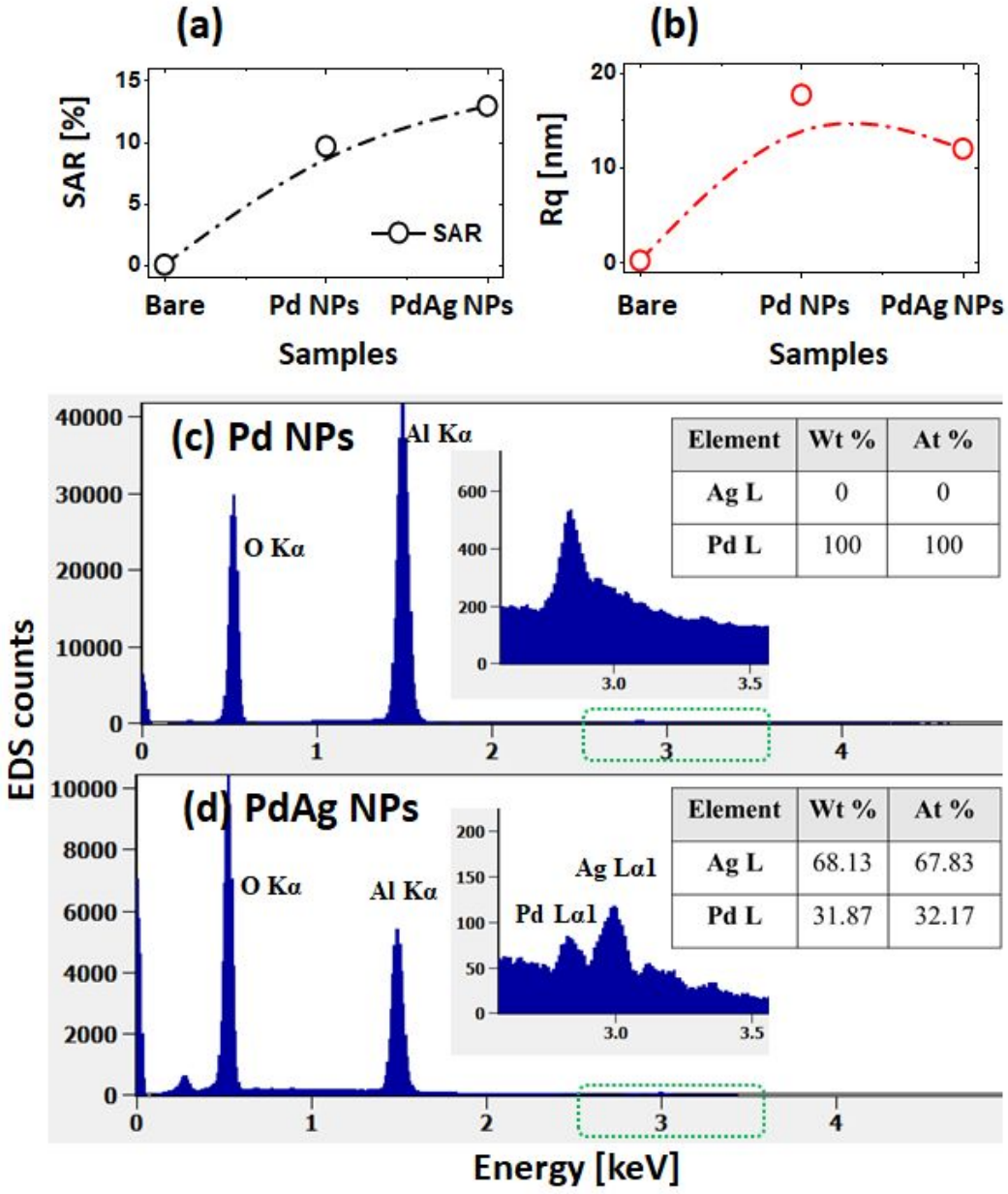

Figure S3. (a) – (b) Summary plots of surface area ratio (SAR) and root mean squared (RMS) roughness (Rq) of bare sapphire, Pd NPs and PdAg HNPs. The SAR measures the increment of 3D surface area of NPs (SA_{NP}) with respect to 2D geometric area (GA_s) as: $SAR = \frac{GA_s - SA_{NP}}{GA_s} \times 100\ \%$ while the Rq provides an average surface height profile (h_i) as: $R_q = \sqrt{\frac{1}{n}\sum_{i=1}^{n} h_i^2}$. (c) – (d) EDS spectra of Pd NPs and PdAg HNPs. The insets show the enlarged peaks of Pd and Ag, which clearly show only Pd peak for the Pd NPs template and Pd and Ag peaks for the HNP sample. The atomic and weight % ratio of Pd and Ag are provided in corresponding inset tables.

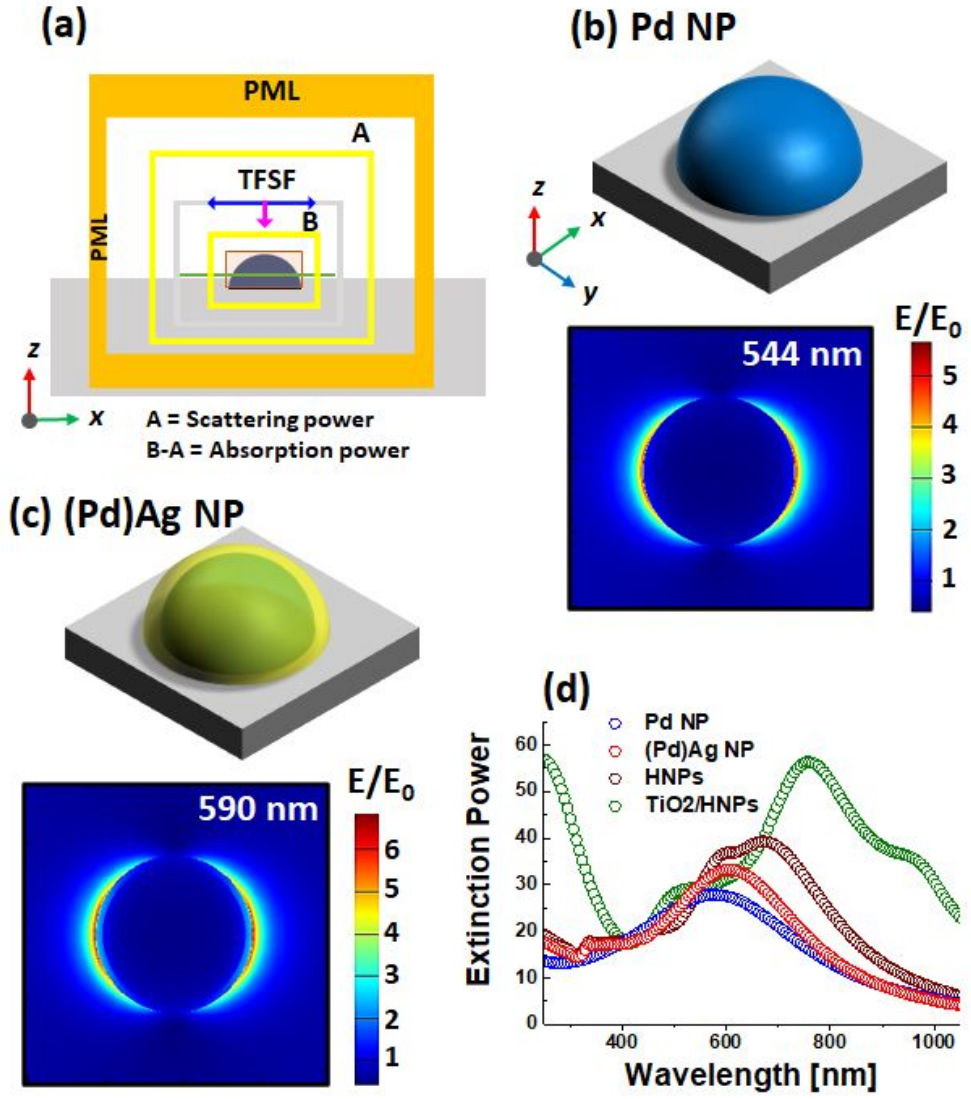

Figure S4. (a) Schematic diagram of the finite difference time domain (FDTD) simulation setup for local e-field distribution and extinction power calculation. (b) – (c) Typical Pd and PdAg core-shell NPs of 120 nm diameter and 50 nm height used for the simulation. The dimension and shape (hemisphere) of the NPs were adjusted based on the AFM images. (d) Calculated extinction power of the pure Pd NP, PdAg core-shell NP, PdAg HNPs and TiO_2/HNP.

The FDTD solution (Lumerical Solutions, Canada) was employed to simulate the e-field distributions of NPs and extinction power calculation. A total field scattered field (TSFS) light source with e-field polarization along x-axis and propagation along z-axis was used as the excitation source above the nanostructure. The absorption and scattering monitors were placed

as shown in the schematic diagram (a) and the extinction power was determined by the relation extinction = absorption + scattering. For the near surface e-field profiles, the DFT monitors are placed at same height (2.5 nm above substrate surface) for each simulation. The spacing between the perfectly matched layer (PML) and the nanostructure was larger than half of λmax. The simulation was carried out with the duration of 1000 fs, auto shutoff level of 1E-6 and mesh size of 0.5 nm in the x, y, z direction. The refractive index of sapphire, Ag and Pd, were fitted from the Palik's and Palm's models [2, 3]. Similarly, the refractive index of the TiO_2 layer was referenced from Siefke's model [4]. In general, the simulated spectra for the typical NPs exhibited a good agreement with the experimental results in terms of peak position, shift and intensity. However, the PdAg HNPs showed red-sift in LSPR peak in contrast to the experimental results. This could be likely due to the disparity in the simulation model and real sample as the high-density Ag NPs were not incorporated in the simulation. In the case of real PdAg HNP sample, due to the collective contribution of the LSPR peak from small Ag NPs, the overall LSPR band can be blue shifted as compared to the large Pd NPs. Another reason for the disparity in the LSPR peak could be the database of the materials. Since the complex refractive index were referred form the previous papers, the mismatch in measurement conditions could cause the minor variation in the simulated response.

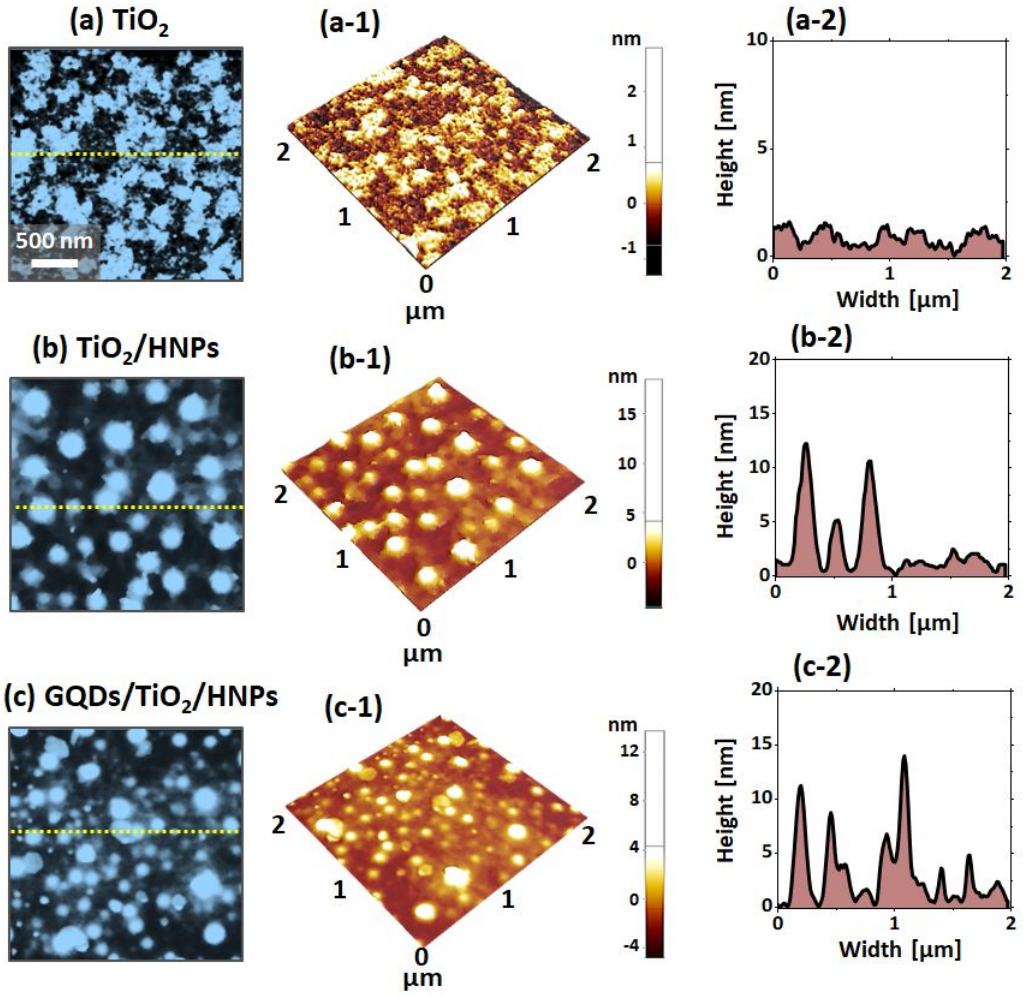

Figure S5. Surface morphology of TiO_2, TiO_2/HNPs and GQDs/TiO_2/HNPs on Al_2O_3. (a) – (c) AFM top-views shows the surface morphology of the samples. (a-1) – (c-1) Corresponding AFM side-views. (a-2) – (c-2) Cross-sectional line profiles as indicated in (a) – (c). The average surface height of TiO_2, TiO_2/HNPs and GQDs/TiO_2/HNPs was gradually increased to 10 and 15 nm respectively.

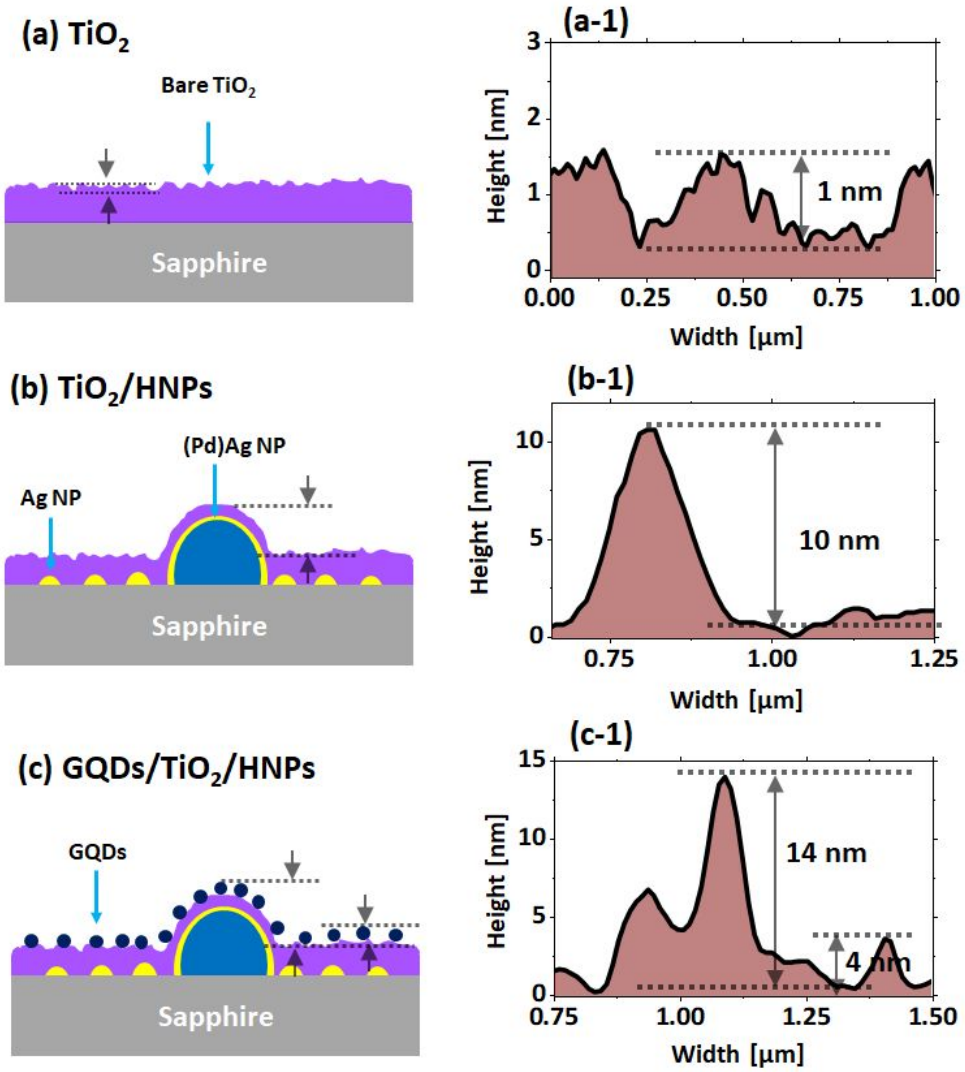

Figure S6. (a) – (c) Schematic illustration of the surface evolution of TiO_2, TiO_2/HNPs and GQDs/TiO_2/HNPs hybrid films along with the deposition of various materials. (a-1) – (c-1) Corresponding cross-sectional line profiles. The TiO_2 film possesses a relatively smooth surface with an average roughness of less than 1 nm. The total thickness of TiO_2 film was estimated to be ~ 40 nm after the deposition of 10 layers. Thus, the large PdAg core-shell NPs (average height 50 nm) were not completely immersed into the TiO_2 layer. The GQDs/TiO_2/HNPs hybrid nanoarchitecture had surface nanoparticles with an average height less than 10 and 15 nm respectively, which could be due to the partially immerged PdAg HNPs and GQDs.

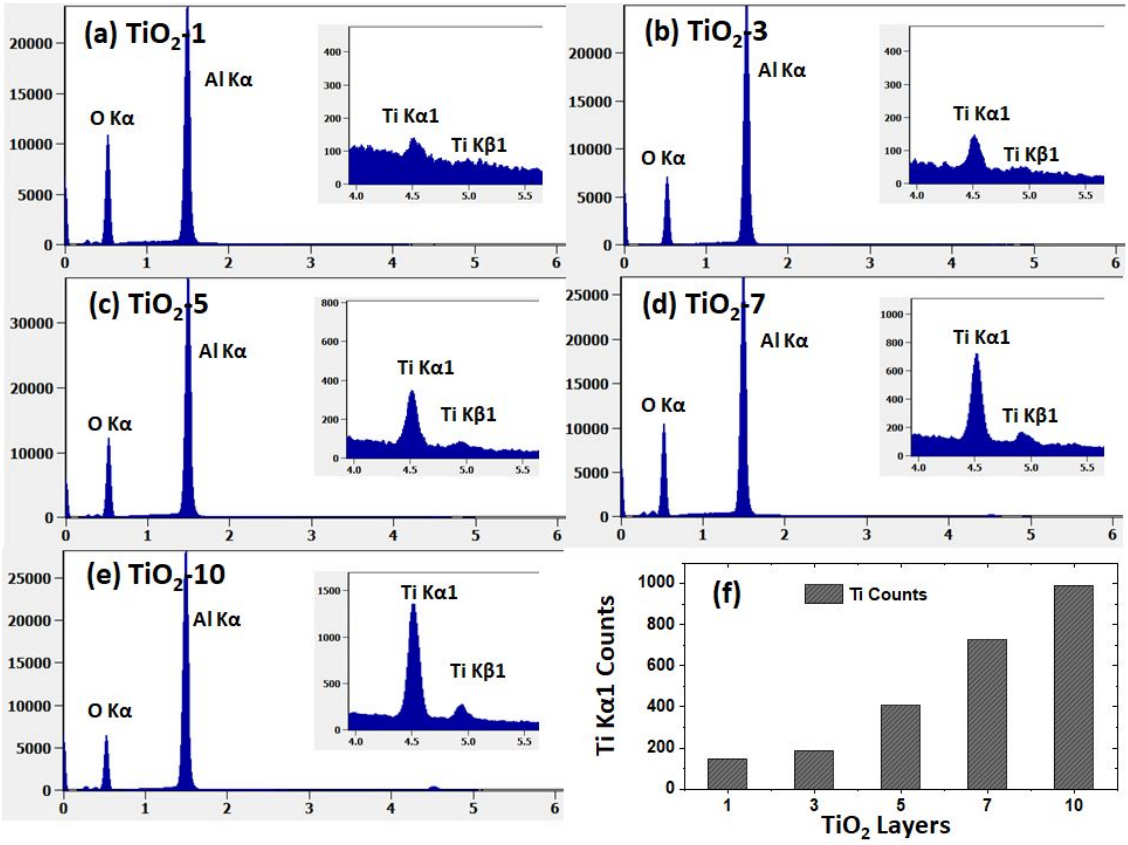

Figure S7. (a) – (e) EDS spectra of various TiO_2-x layers on sapphire (0001), where the x denotes the number of layers. Insets show the enlarged peaks of Ti Kα1 and Ti Kβ1 for a different number of TiO_2 layers. (f) Summary of Ti Kα1 counts with respect to the number of layers. The intensity of Ti peaks and EDS counts is successively increased with the addition of TiO_2 layers.

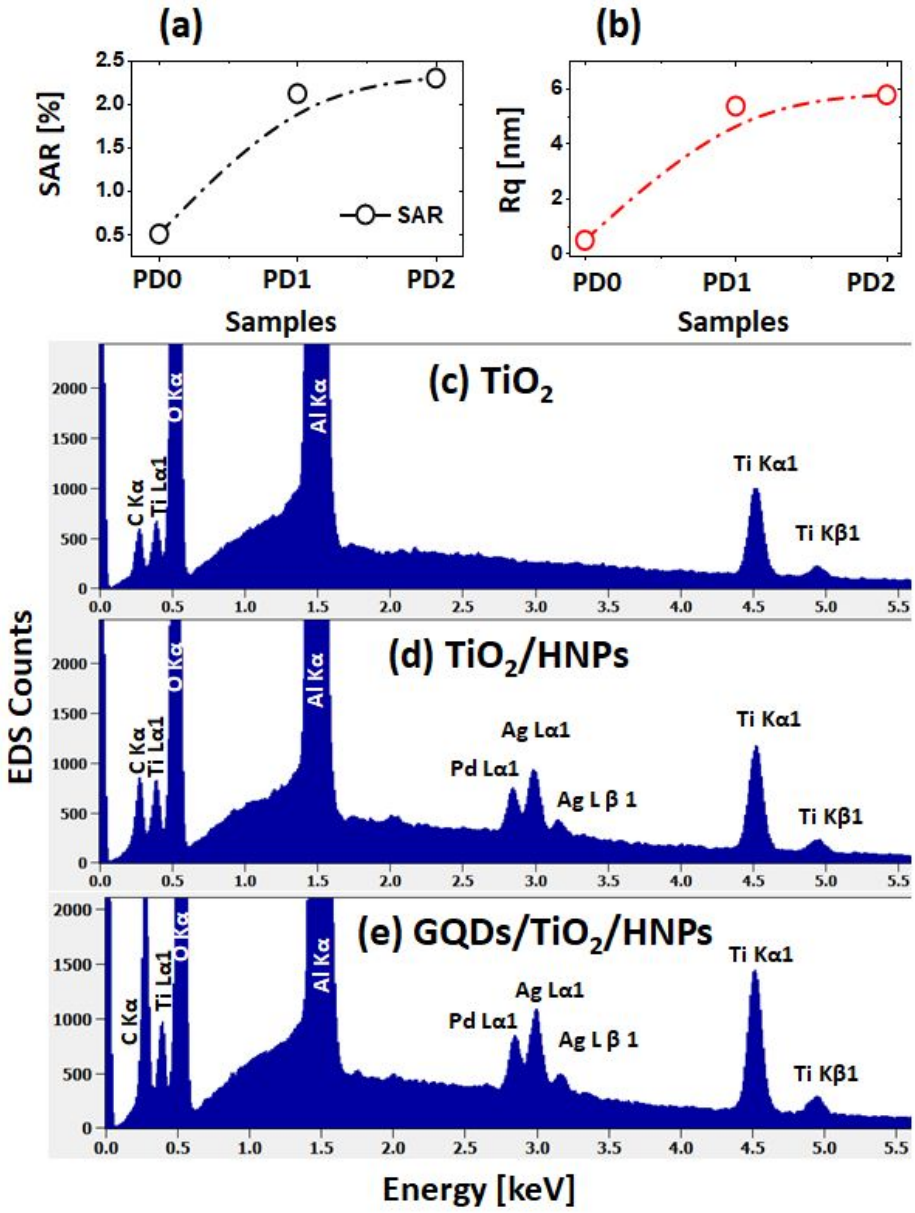

Figure S8. (a) – (b) Summary plots of SAR and Rq of TiO_2, TiO_2/HNPs and GQDs/TiO_2/HNPs hybrid films. (c) – (d) EDS spectra of corresponding samples.

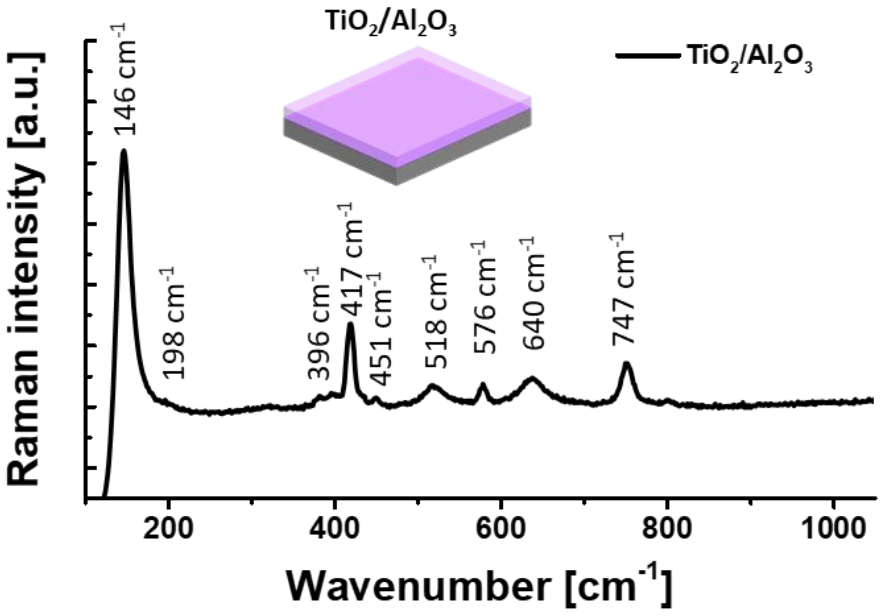

Figure S9: Raman spectra of TiO_2 fabricated on sapphire. The active Raman modes of TiO_2 are at 146 (E_g), 198 (E_g), 396 (B_{1g}), 518 (A_{1g}/B_{1g}) and 640 (E_g) cm^{-1} while the other peaks at 417 (A_{1g}), 451 (E_g), 576 (E_g) and 747 (E_g) cm^{-1} corresponds to sapphire (Al_2O_3) [5]. The Raman peaks of the TiO_2 indicates the formation of anatase phase.

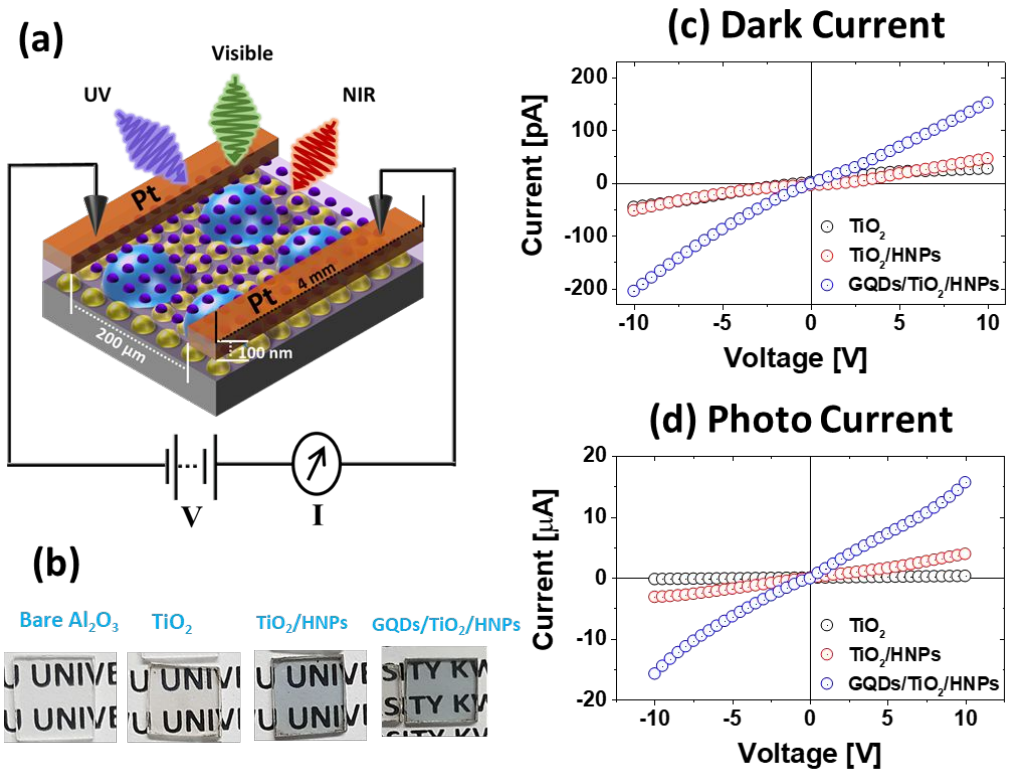

Fig S10. (a) Schematic of the GQDs/TiO_2/HNPs hybrid photodetector. The active region, channel length and platinum (Pt) electrode thickness were 200 µm, 4 mm and 100 nm respectively. (b) Digital camera photograph of bare sapphire (Al_2O_3), TiO_2, TiO_2/HNPs and GQDs/TiO_2/HNPs samples. (c) Current-Voltage (I-V) characteristics of 3 devices under dark condition. (d) I-V characteristic of each device under the illumination of 275 nm UV light at 1.64 mW/mm^2.

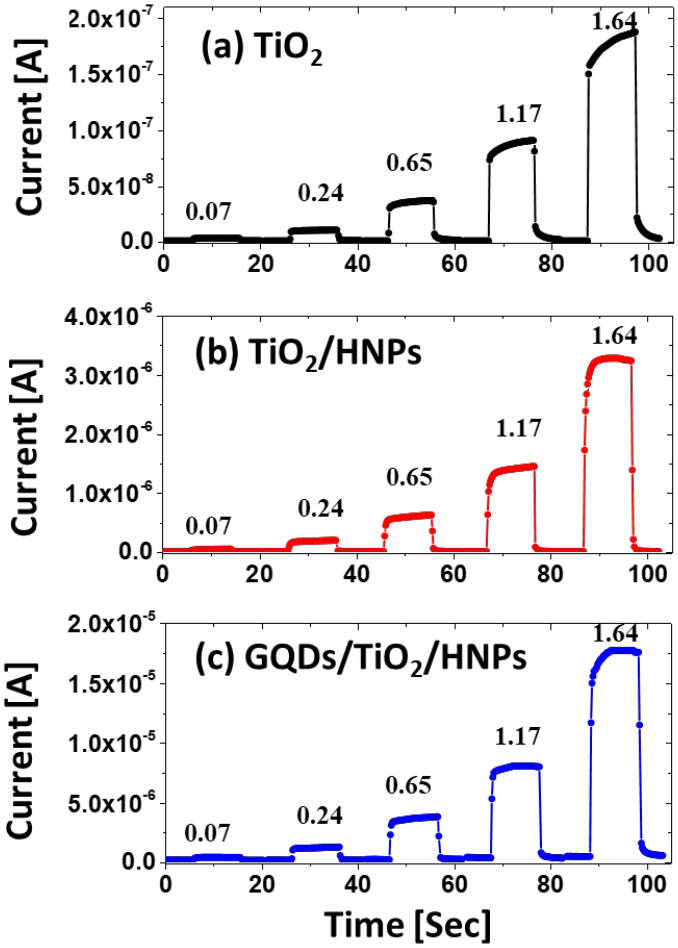

Figure S11. (a) – (c) Power dependent photoresponse of the TiO_2, TiO_2/HNPs and GQDs/TiO_2/HNPs photodetectors at fixed 10 V bias. The light intensity of the 275 nm LED was fixed at 1.64 mW/mm^2. The photocurrent of the device is successively increased with the illumination power.

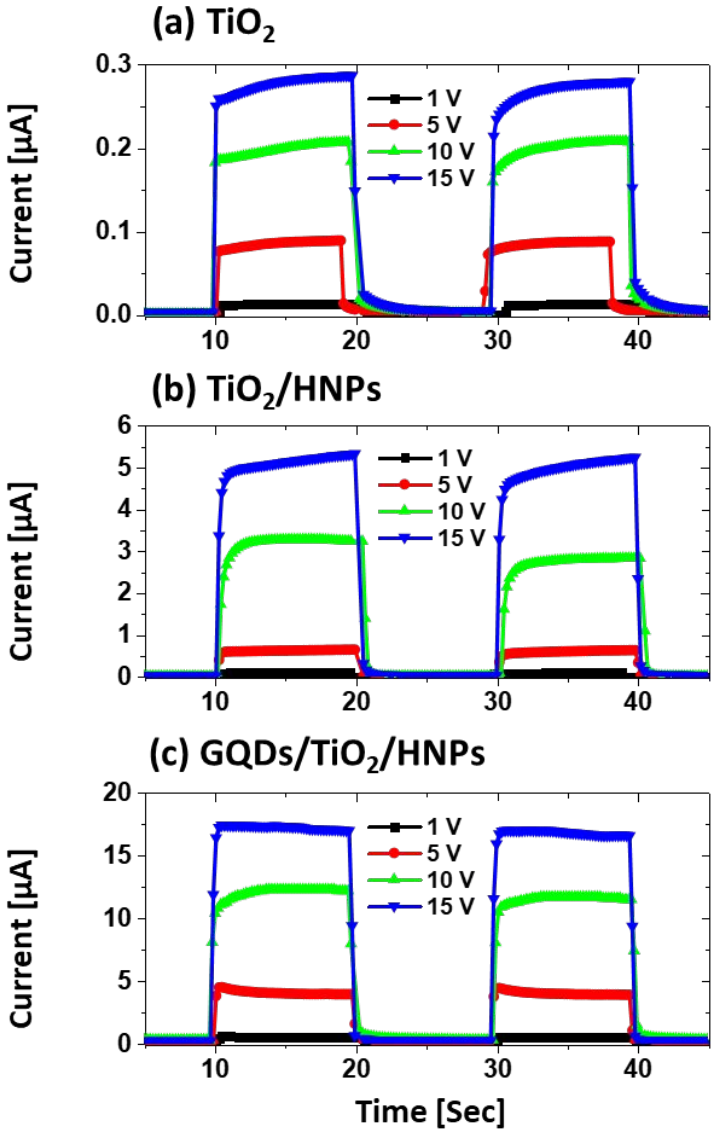

Figure S12. (a) – (c) Voltage variation effect on the photoresponse of TiO_2, TiO_2/HNPs and GQDs/TiO_2/HNPs at fixed UV illumination (275 nm, 1.6 mW/mm^2). The photodetector devices showed stable photocurrent response at different voltage between 1 and 15 V.

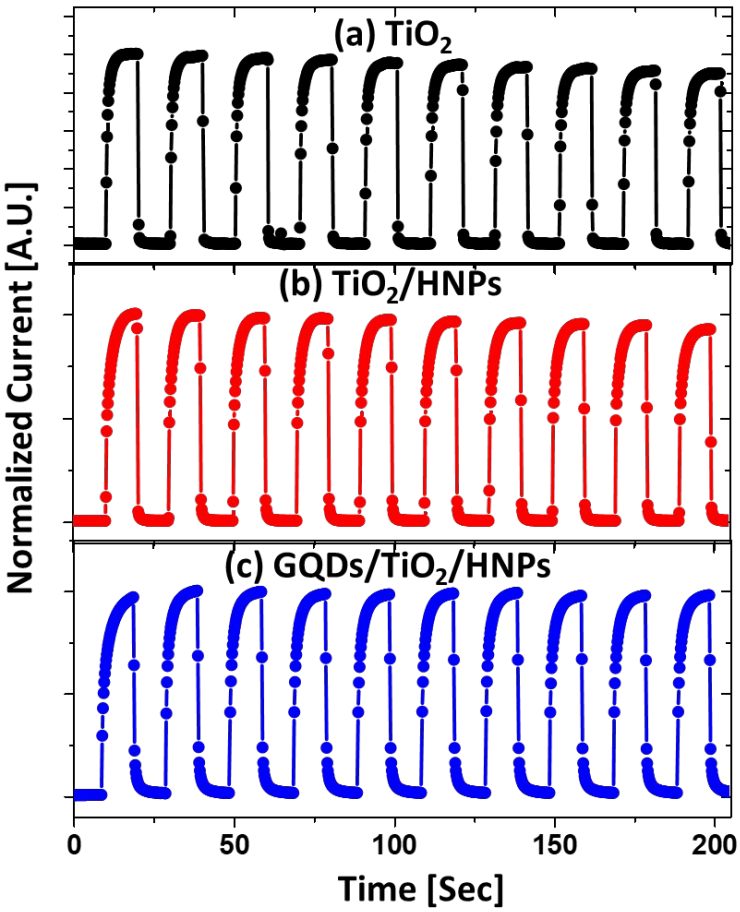

Figure S13. (a) – (c) Time-resolved photoresponse of the TiO_2, TiO_2/HNPs and GQDs/TiO_2/HNPs at 10 V under multiple on/off cycle of UV (385 nm, 10.36 mW/mm^2). The photodetectors exhibited good stability and repeatability of the photoresponse pulse upon UV on/off.

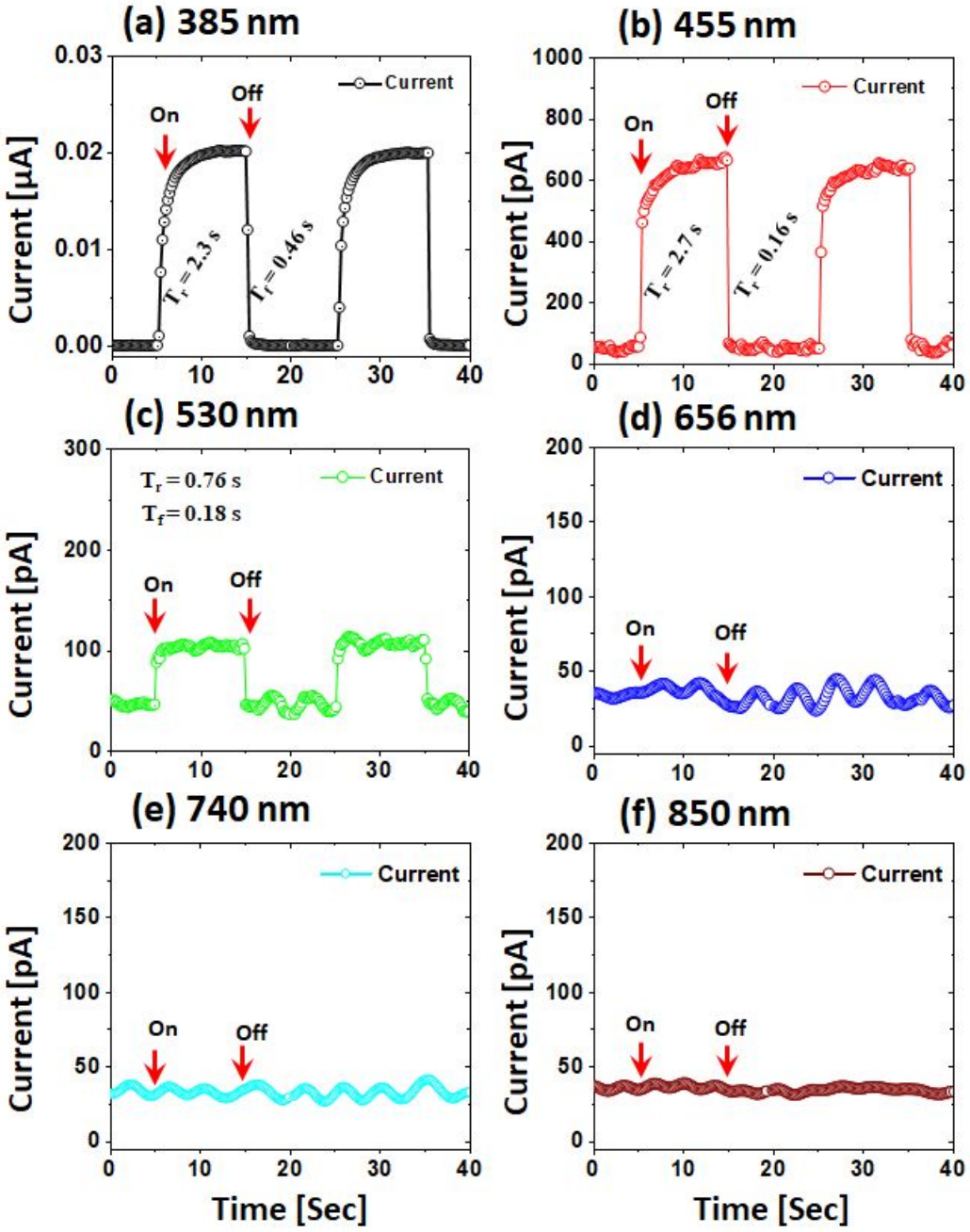

Figure S14. (a) – (f) Time-resolved photoresponse of TiO_2 photodetector with various illumination wavelengths between UV and NIR regime.

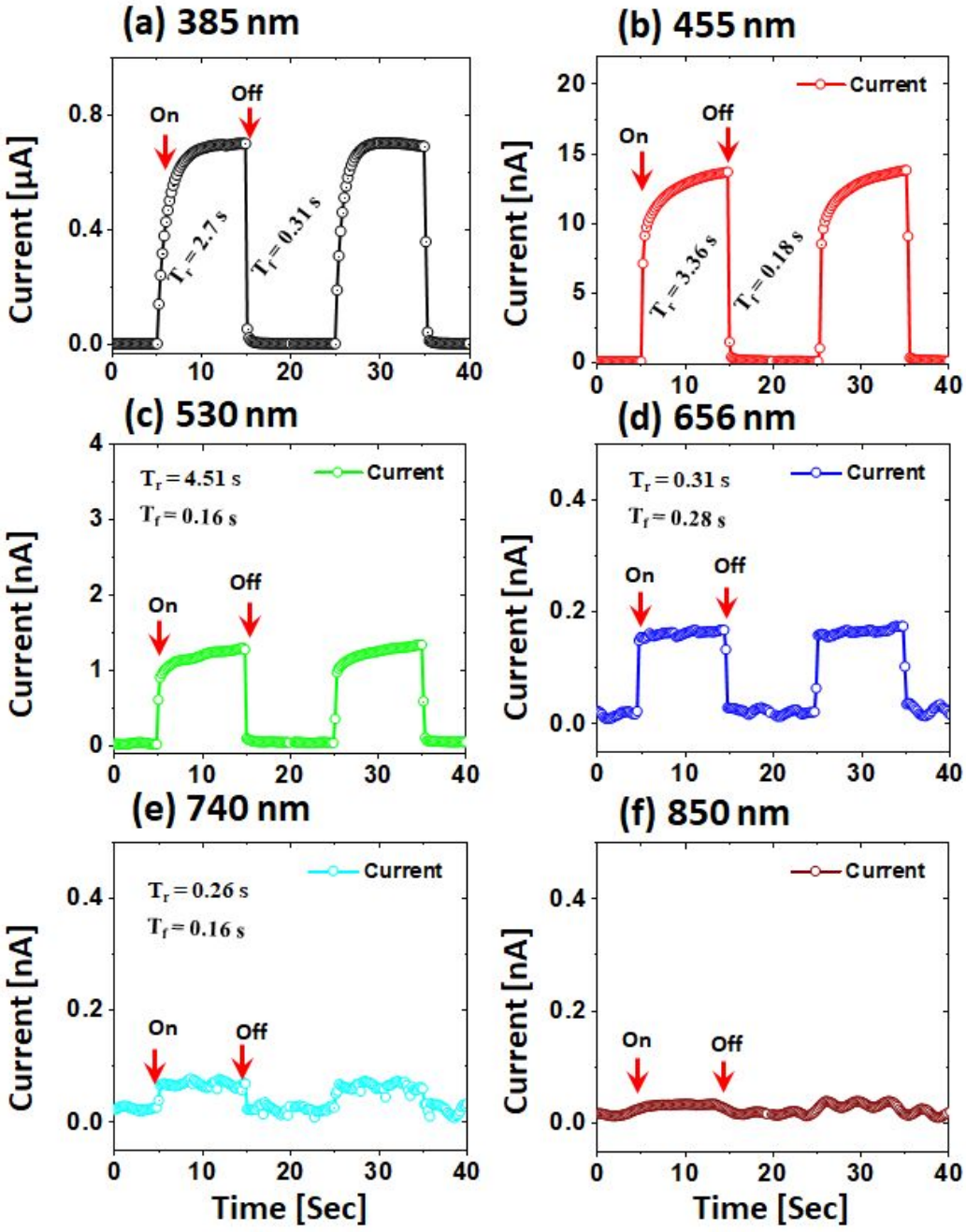

Figure S15. (a) – (f) Time-resolved photoresponse of the TiO_2/HNPs hybrid photodetector with various illumination wavelengths between UV and NIR regime.

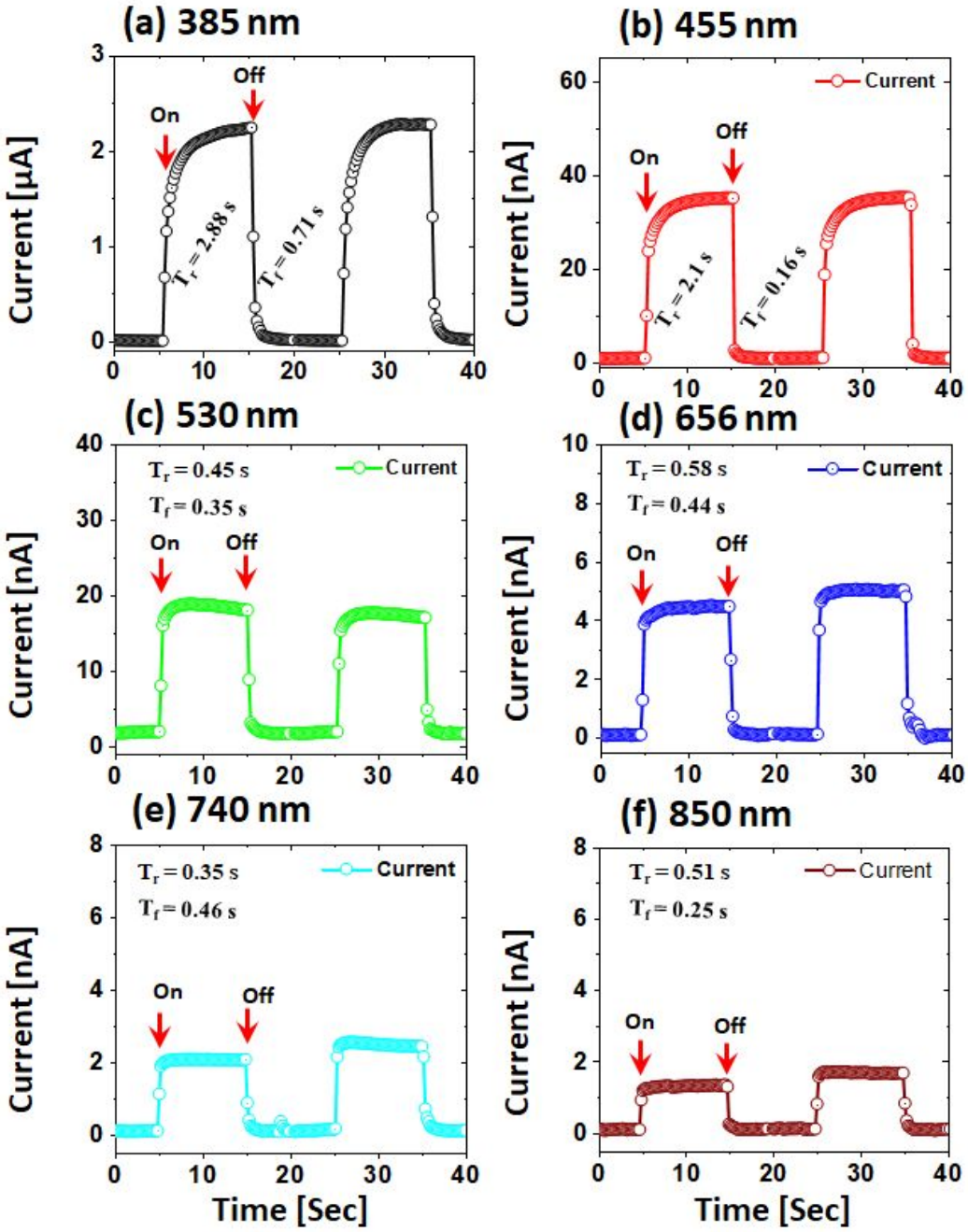

Figure S16. (a) – (f) Time-resolved photoresponse of the GQDs/TiO_2/HNPs with various illumination wavelengths between UV and NIR regime.

Table S1. Summary of average extinction and peak position of various TiO_2-x layers between 1 and 10 on bare sapphire and on the HNPs template. The TiO_2-10 is denoted as TiO_2 for the simplicity in the device names. Finally, one layer of GQDs was added on the TiO_2 layer in each case.

TiO_2 layers	**Average Extinction**		**Peak positions with NPs**
	TiO_2	**TiO_2/HNPs**	
TiO_2-1	1.18	21.01	549.91
TiO_2-3	1.46	25.74	559.43
TiO_2-5	1.43	27.96	560.59
TiO_2-7	2.02	28.76	574.23
TiO_2	3.61	29.18	611.35
GQDs/TiO_2	9.76	32.02	581.84

Table S2. Summary of the responsivity (R), of the TiO_2, TiO_2/HNPs and GQDs/TiO_2/HNPs photodetectors as a function of power variation of UV (275 nm) illumination at a constant bias of 10 V.

Power [mW/mm²]	**R [mA/W]**		
	TiO_2	**TiO_2/HNPs**	**GQDs/TiO_2/HNPs**
0.077	0.22199	3.84	28.31
0.24	0.21946	4.25	28.72
0.65	0.28401	4.79	30.63
1.17	0.38678	6.18	34.43
1.64	0.57162	10	54

Table S3. Summary of the detectivity (D) of TiO_2, TiO_2/HNPs and GQDs/TiO_2/HNPs photodetectors as a function of power variation of UV (275 nm) illumination at a constant bias of 10 V.

Power [mW/mm²]	**D [jones]**		
	TiO_2	**TiO_2/HNPs**	**GQDs/TiO_2/HNPs**
0.077	3.12E9	4.63E10	1.79E11
0.24	3.09E9	5.12E10	1.78E11
0.65	3.99E9	5.78E10	1.90E11
1.17	5.44E9	7.45E10	2.14E11
1.64	8.04E9	1.21E11	3.35E11

Table S4. Summary of the *R* of TiO_2, TiO_2/HNPs and GQDs/TiO_2/HNPs photodetectors based on the bias variation at 1.64 mW/mm^2 of UV (275 nm) illumination.

Voltage [V]	Responsivity [mA/W]		
	TiO_2	**TiO_2/HNPs**	**GQDs/TiO_2/HNPs**
1	0.040	0.35	1.96
5	0.27	1.96	13.78
10	0.57162	10	54
15	0.87	16.24	58.5

Table S5. Summary of the *R* of the TiO_2, TiO_2/HNPs and GQDs/TiO_2/HNPs as a function of wavelength between UV, VIS and NIR regime at fixed 10 V bias.

Wavelength [nm]	**Responsivity [mA/W]**		
	TiO_2	**TiO_2/HNPs**	**GQDs/TiO_2/HNPs**
275	0.572	10	54
385	0.007	0.12	1.68
455	2.19E-4	0.0124	0.03
530	6.24E-5	0.00261	0.014
656	0	1.35E-4	0.0072
740	0	1.42E-4	0.011
850	0	0	0.0035

References

1. M. Kadleíková, J. Breza, and M. Veselý, Microelectronics J. **32**, 955 (2001).

2. K. J. Palm, J. B. Murray, T. C. Narayan, and J. N. Munday, ACS Photonics **5**, 4677 (2018).

3. Palik, E.D. ed., 1998. Handbook of optical constants of solids (Vol. 3). Academic press.

4. T. Siefke, S. Kroker, K. Pfeiffer, O. Puffky, K. Dietrich, D. Franta, I. Ohlídal, A. Szeghalmi, E. B. Kley, and A. Tünnermann, Adv. Opt. Mater. **4**, 1780 (2016).

5. E. S. Araújo, J. Libardi, P. M. Faia, and H. P. De Oliveira, J. Chem. **2015**, (2015).